How CFD-DEM Simulations benefit from Machine Learning

Stefan Radl,* Hadie Benabchiasli,* Gregor Fasching,* Michael Mitterlindner,* and Mohammadsadegh Salehi*,**

radl@tugraz.at

Graz University of Technology, Institute of Process and Particle Engineering, 8010 Graz
** Virtual Vehicle Research GmbH, 8010 Graz

Abstract

Computational Fluid Dynamics-Discrete Element Method (CFD-DEM) simulations have become a valuable tool in industry and academia. In the context of combustion systems, CFD-DEM simulations are mainly relevant as tools for basic research, e.g., to understand phenomena such as segregation or other effects due to incomplete (particle) mixing. Typically, such simulations face the following challenges: (i) modelling of complex-shaped and deformable/shrinking particles, (ii) considering (cohesive) particle interaction forces that might change during the combustion process, or (iii) predicting (radiative) energy transfer rates that are sensitive to a large number of parameters that are almost impossible to measure directly. All these challenges have in common that a large number of predictions (or decisions) have to be made in a short time, and that these predictions depend on a large number of inputs ("features") in a non-trivial way. Machine Learning (ML)-based algorithms are promising candidates to tackle these challenges.

In our present contribution we highlight three concrete examples of how ML-empowered CFD-DEM simulations can be realized: (i) ML for closure construction in the field of particle-particle radiative energy transfer [1], (ii) ML-empowered drag force modeling [2], as well as (iii) ML-aided calibration workflows for advanced parameter identification in the context of granular flow and bulk heat conductivity prediction using CFD-DEM. We will conclude our talk with an application study of a problematic reactive granular material encountered in industrial NiMH battery recycling.

Introduction

CFD-DEM simulations in the field of industrial combustion processes are intrinsically multi-physics applications. In the following we briefly highlight three areas which are the most essential to understand for our current contribution.

(1) Energy transfer and reactions – the need for CFD-DEM

As summarized in the review article by Mahiques et al. [3], relevant application cases in the field of combustion processes are characterized by complex particles shapes, a dynamic (i.e., conversion-dependent) particle size distribution, and a resulting complex particle flow behavior. The environment experienced by an individual particle determines its properties, resulting into challenges for Eulerian methods. The (classical) strength of the CFD-DEM approach lies in applications with comparably large particles, since there is hope that individual particles can be described. This matches with applications for thermally thick particles, for which particle tracking is essential and intra-particle gradients (e.g., of the temperature) must be resolved. In this field, the calibration of single-particle models is state of the art. Remaining challenges are the modeling of conductive heat transfer and radiation phenomena, as well as the prediction of particle flow related issues (e.g., bridging & arching, or segregation). Last, simulation time is a key issue, with particle flow prediction being a dominating sink of computing resources. Limited simulation time also motivated our previous work on accelerated view factor calculations [1], which used machine learning to make fast and precise predictions.

However, there is no fundamental need to track individual particles in CFD-DEM: parcel-based approaches [4] can be used, in which not all particles are followed by the DEM. An example would be the combination of a parcel-based DEM with a "representative particle" approach (e.g., as followed by Wurzenberger et al. [5]). Especially for such a parcel-based DEM one needs to find suitable particle parameters to be able to make realistic predictions. Next, we review how such a calibration can be done.

(2) Momentum transport within the particle phase - Calibration of DEM parameters

The basic idea of calibration is to account for effects that cannot be directly measured (e.g., particle roughness, cohesion forces, deformation of individual particles), or would require excessive calculation resources (e.g., a wide particle size or shape distribution). In the field of calibration, one has to separate

between (i) "free flowing" (i.e., cohesionless) particles [6], and (ii) cohesive particles [7][8]. Also, it is of importance for which flow situation the DEM model should be calibrated (e.g., slow versus fast flows [9], or low versus high stress applications [10]). There has been a strong increase of publications related to calibration of DEM parameters in recent years. This is caused by (i) the maturity of simulation tools, and (ii) the semi-automated processing of experimental data that is nowadays often collected with inexpensive cameras. Last but not least, advances in (machine) learning algorithms have made calibration tools more reliable and efficient. Also, our current contribution is motivated by these advances, and we have included our most recent results from an application study in the field of battery recycling.

(3) Momentum transfer between the phases - drag modification

Moderately dense gas-particle system involving particles in the range of 50 to 1000 μm in diameter (typical for fluidized bed applications) spontaneously form cluster when flowing [11]. An approach to quantify the effect of cluster are so-called "filtered" drag models, which are also relevant for CFD-DEM models [12]. The methodology of filtered drag model development has long suffered from the interpretation of the filtered data, and tedious manual fitting of closure relations. Recently, machine learning has also been applied to this field of research [2,13], greatly accelerating research and increasing the models' fidelity. For example, it is now possible to create an anisotropic drag correction model within hours of machine learning time, which would have taken several weeks if parameterized by hand.

Goals

The goal of our current overview paper is two-fold:

(1) We summarize machine learning strategies, as well as highlight tools for machine learning that we have previously used, and which are relevant for CFD-DEM simulations in the field of combustion. We will focus on the view factor example in our present study here.

(2) Show an application of ML-based calibration to model poorly flowing material as typical for the energy sector. Specifically, we document results of a material encountered in NiMH battery recycling. Here our focus is on the calibration of a DEM-based model for flowability prediction. We also give a short preview on how to parameterize the DEM-based model such that it is useful for heat conduction predictions.

Overview of Learning Strategies & Learning Tools used

In what follows we focus on so-called "supervised" learning strategies (see Zhu et al. [14] for an excellent review of the field). The goal when following such a strategy is to learn correlations from an existing data set (i.e., a plurality of data points consisting of multiple markers or "features" that characterize one or more "targets"). An example is to use the relative position data (and other information about the local packing) in a particle packing to estimate view factors between two particles [1]. Certainly, unsupervised strategies (e.g., clustering via a k-Means approach) can be used in advance in situations in which markers to be used are not known a priori. As this was not the case for our applications, we will not further detail such an unsupervised learning strategy. Certainly, unsupervised learning can be a powerful tool for dimensionality reduction, translating into a reduction of the input complexity for supervised learning.

In some fields of research (e.g., clustered gas-particle suspensions) experimental data is not available, or not available in enough detail. Hence, one must rely on simulated data for learning. In such a situation it is important to carefully verify and validate the simulator, and subsequently select a suitable simulation setup is. Figure 1 illustrates this need: specifically, we here summarize our strategy for the development of closures in our previous work on drag and view factors. Here the "x-physics simulator" indicates any multiphysics simulator used on top of a CFD and/or DEM simulation (e.g., a ray tracing simulator to determine view factors). When adopting such a strategy, it is important that (i) closures should be formulated in dimensionless form (otherwise machine learning tools will normalize data in a possibly inappropriate way), and that (ii) closures are designed to automatically respect limiting cases (e.g., no clustering corrections for the drag in the dilute and dense limit). For learning from data when following strategy I illustrated in Figure 1, we used the open-source Keras® tool that runs on a Tensorflow core. We access this tool via a Python interface. Furthermore, the resulting neural networks can be easily combined with an existing C++-codebase (e.g., via https://github.com/pplonski/keras2cpp/). Another popular choice would be PyTorch (https://pytorch.org), or scikit-learn (https://scikit-learn.org).
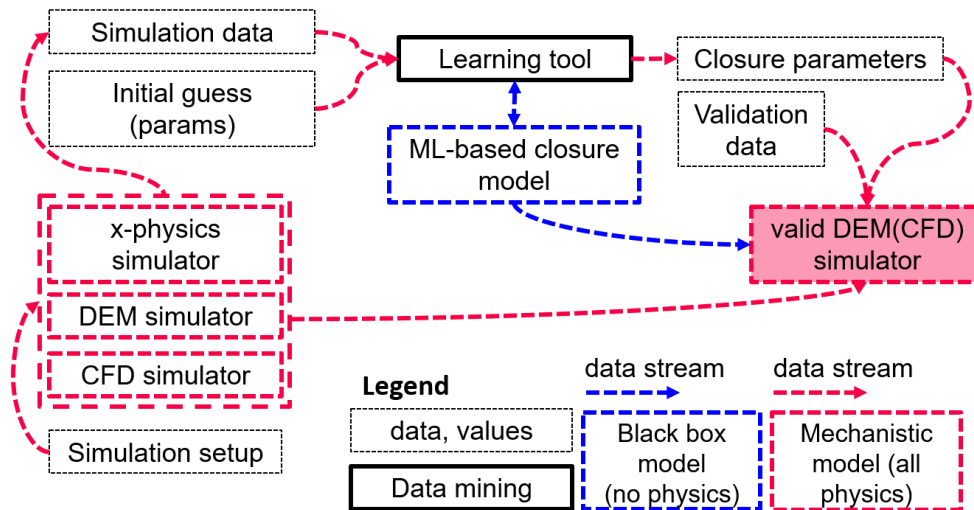
Figure 1. Learning strategy I: learning from (filtered) simulated data via a grey-box approach.

In the field of DEM-based simulators for (dense) particle flow, the available experimental data set is typically scarce (i.e., a few hundred datapoints at most). Also, typical machine learning models (e.g., neural nets) are not used: in contrast the parameters in a mechanistic model need to be predicted. Thus, the structure of the model to be trained is relatively rigid (i.e., the closure is typically fixed, e.g., for the normal contact force the stiffness needs to be determined). This different scenario leads to an entirely different learning strategy as shown in Figure 2: these learning strategies are referred to as "calibration", since only a handful parameters (at most) need to be determined. Two classes of calibration strategies exist: (i) in **response surface-based methods** only DEM models & parameters covered by a pre-computed response surface can be calibrated. This method is relatively rigid (i.e., the update of simulation model will result in the need for the entire re-evaluation of the response surface). The advantage is that DEM simulations run only once for a combination of parameters. After these simulation runs a learning tool (index A) is used to create the response surface (in the simplest case this tool uses linear interpolation in the precomputed dataset). Consequently, during the calibration step no DEM simulations are needed, and hence this step is fast. The intersection of the generated response surfaces for multiple setups to match experimental data is handled by a second learning tool (index B; this tool is preferably implemented in the same software as learning tool A). Note that in this strategy a black box model needs to be involved, and hence care has to be taken to ensure that extrapolations are handled in a meaningful way. (ii) a more flexible methodology (i.e., **direct calibration**) that does not require any black box model is illustrated in Figure 2b: any DEM model can be used that is available in the simulation, and a small amount of DEM simulations must be run for each calibration job. The learning tool is here reduced to an optimization algorithm - which is the heart of this calibration workflow - and attempts to minimize a loss function. In case multiple targets need to be matched, experimental datasets can be used for calibration in a sequential way. Alternatively, a loss function is constructed by considering multiple targets. In our case study on NiMH recyclate processing we use the strategy shown in Figure 2b. As software we have chosen the tool Aspherix© Calibration.
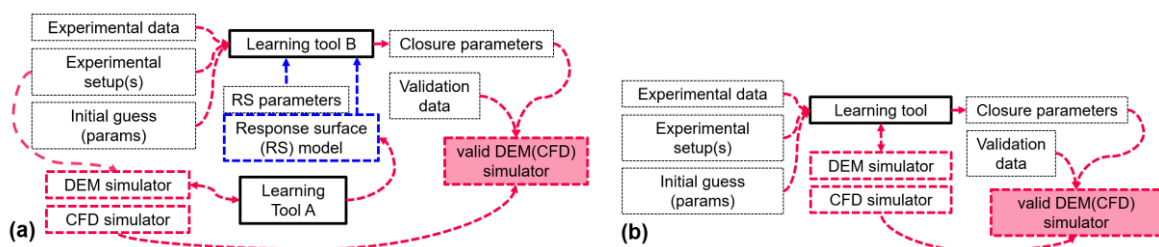

Figure 2. Learning strategy II: response surface-based calibration of closure parameters (a, left), as well as direct calibration of closure parameters (b, right) for (CFD)-DEM simulators.

We note in passing that combining the ideas of the "response surface" method and sequential calibration of parameters is possible: a recent example for such an approach is the study of Carr et at. [8].

Results

Radiative Energy Transfer between particles – View Factor Predictions

For this application we here highlight the use of neural networks (NNs) as illustrated in Figure 3: these networks are conceptually simple learning models, a relatively small amount of data needs to be saved, and they have shown to represent our data in an excellent way. Note, so-called random forest regressors may perform better (better prediction, faster training) compared to NNs for some applications [1].
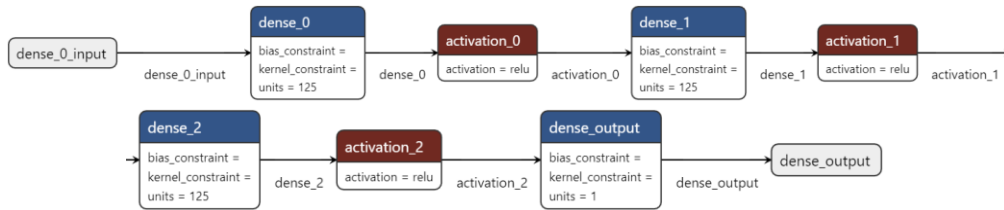

Figure 3. Typical layout of a neural network used for the prediction of view factors (data from Tausendschön [15] for particle-wall interactions, visualization with Netron [16]).

While training and validation were already published elsewhere [1,15,17], we here highlight some interesting predictions for view factors in dense mono-disperse granular packings. Specifically, we here test whether the trained model respects limiting cases, and makes robust predictions even when forced to extrapolate. Results for such a check are shown in Figure 4: specifically, we extrapolate outside of the calibration data range for the particle concentration (i.e., the particle volume fraction range for calibration was $\phi_{p,calib} = [0.199, 0.554]$, while we here use $\phi_p = [0.1, 0.60]$, see Figure 4). Also, we make an extreme abuse of the resulting neural network by assuming a large number of shadowing particles n_{bip} even at small separation distances $|x_{ij}|$. As can be seen in Figure 4, we do respect the limiting case for contacting particles (indicated as dash-dotted line at a view factor of ε_{ij} = 0.0762) very closely if there are no shadowing particles (i.e., n_{bip} = 0). The extreme abuse with n_{bip}=30 (dashed lines) yields still reasonable results, however, is already -34% off the limiting case. Fortunately, if we use a reasonable number of shadowing particles $n_{bip,reas}$ (we assume that an integer number of particles fills the gap between the two particles once it is large enough; see the thin lines in Figure 4 which indicate sudden jumps at $|x_{ij}|/r$ = [4, 6, 8] due to this "gap filling"), the neural network predicts correct view factors that are in between the extrema, again leading to a close match with the limiting case.
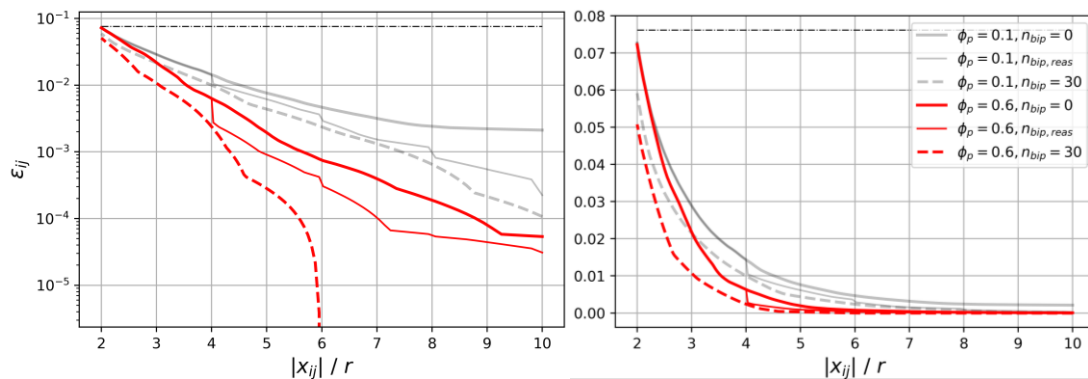

Figure 4. Predicted particle-particle view factors for a monodisperse packing for a dilute case (i.e., $\phi_p = 0.1$; black low opacity lines) and a dense case ($\phi_p = 0.6$, red lines; the black dash-dotted line is the reference result for contacting spheres located at $|x_{ij}|$ = 2·r. Neural network from Tausendschön [15]. Left: log-scale on the y-axis, right: linear scales).

DEM parameters for NiMH Battery Recyclate Modeling - Flow

We now move on to the topic of parameter learning (or "calibration") for DEM-based models. We start with the description of the experimental setup that is used in our lab to gather the necessary training and validation data.

Experimental Details
Experimental details are summarized here only in brief: a draw down test box (see Figure 6c) was constructed that allows us to realize various opening sizes between an upper and a lower box. The exact geometry was motivated by prior work [18]. For each opening size, a draw down test with the material (industrial NiMH recyclate material) was performed 6 times. The mass of the recyclate material in the lower box after each experiment was noted (equaling the "mass loss"), together with qualitative information for the experiment (i.e., arching occurring or not). Furthermore, image analysis techniques have been used to determine the shape of the bottom pile after each experiment (image processing was performed with Fiji [19] and Octave, https://octave.org/). For both results, i.e., the mass loss and the shape of the pile, data was averaged over individual realizations for subsequent analysis and calibration.

Method and Model Details
Machine learning (i.e., calibration of DEM parameters) was realized with the Aspherix® Calibration tool. Due to the nature of the material (recyclate consisting mainly of fluff with interspersed small particles with a typical size of 10 micros), we are forced to use a coarse-grained DEM approach. Also, the plurality of fibre and particle shapes was entirely neglected, at the cost of not being able to simulate segregation phenomena.

For all simulations, relatively standard contact model closures implemented in Aspherix® were used (model and implementation details widely match that of the open-source DEM simulator LIGGGHTS [20,21]). Specifically, this was a Hertz contact model with friction (and tangential overlap tracking). To account for the cohesivity of the particles, the SJKR model was used (this sub-model was also the target for calibration as discussed below). The rolling resistance of the particles was modelled using the modified elastic-plastic spring-dashpot model. Additionally, the keyword "limitForce" was used to prevent attractive non-cohesive forces between the particles and between particles and the walls (this is important since we used comparably strong damping of contacts as indicated by the small coefficient of restitution). All DEM input parameters needed for the use of the specified model are listed alongside their respective value in Table 1.

Table 1. Fixed DEM parameters used in our calibration simulations.

Parameter (P = Particle, W = Wall)	Value	Unit
Young's modulus Y [P, W]	1e8	[Pa]
Poisson ratio ν [P, W]	0.30	[-]
Coefficient of restitution e [PP, PW]	0.30	[-]
Sliding friction coefficient μ_{pp} [PP]	0.71	[-]
Sliding friction coefficient μ_{pw} [PW]	0.41	[-]
Rolling friction coefficient μ_r [PP,PW]	0.80	[-]
Density ρ_p [P]	3400	[kg/m³]

Calibration simulations were performed where the important parameter, i.e., the cohesion energy density k_{sjkr}, was varied until the shape of the pile matched that of the respective experiment (this was realized with the learning algorithm implemented in Aspherix® Calibration). It is important to note here that all other DEM input parameters reported in Table 1 were preset with values mostly taken from [9]. The opening size of 250 mm was used for the calibration procedure as it was the smallest opening size used during the experiments. In all 6 experimental runs for the opening size of 250 mm, arching was observed. Also, it is important to note here that in all calibration cases, the particle-wall cohesion interactions have been set to zero (preliminary simulations with activated particle-wall cohesion yielded excessive sticking, which was not observed in the experiments).

To validate the determined value of the cohesion energy density, the same value of the cohesion energy density was used for simulations of experiments with opening sizes of 320 mm and 400 mm. For the opening size of 320 mm, arching occurred for 4 out of 6 experiments; for the opening size of 400 mm, arching never occurred and almost all of the recyclate material fell from the top box into the lower box.

To quantify the success of calibration, the relative difference m_{rel} defined by $m_{rel} = \frac{abs(m_{exp} - m_{sim})}{m_{exp}}$ was used. In this equation, m_{exp} and m_{sim} stand for the mass in the lower box after the experimental and simulation run, respectively. It is important to note here that for an accurate calculation of m_{rel}, the density of the particles has to be varied each time a different cohesion energy density is used [22]. This is due to the fact that the cohesion energy density influences the particle volume fraction ϕ_p, and consequently how many particles fit into the upper box.

Preliminary Calibration Runs with Spheres
For our first set of calibration runs we considered spherical particles since this is the most obvious choice (computational reasons, only one geometry parameter). In our case we considered monodisperse spherical particles with a diameter of $d_p = 8\,[mm]$. Calibration of the cohesion energy density with otherwise fixed interaction parameters was performed with the target being the (average over 6 realizations of each experimental setting) shape of the bottom pile (see Figure 5 for an illustration of the target and its match with the simulation data). This shape was expressed as the average width-versus-height profile of the forming pile. We note in passing that this is an elegant choice, since it combines information about the angle of repose with a metric for the mass that has left the upper box.
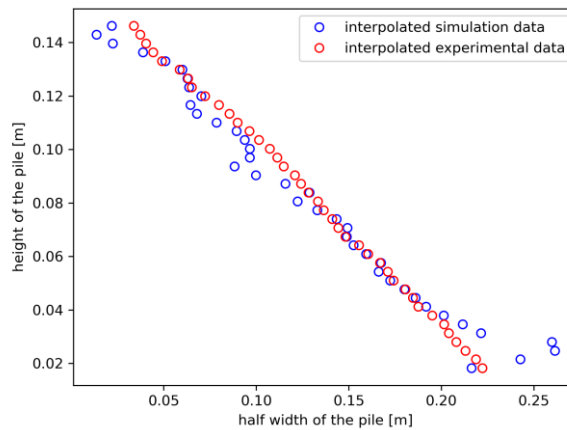

Figure 5. Illustration of the target matching strategy during learning of DEM parameters.

The cohesion energy density was gradually increased in an attempt to replicate the arching behavior of the experiments for an opening size of 250 mm. Figure 6a shows the final state of the particles after they have settled when a cohesion energy density of $4 \cdot 10^5$ [J/m³] was used. Note that absolutely no arching did occur in contrast to the experiments as documented in the section "Result of Calibration and Validation with Tetrapods" below. Thus, the approach to use spheres was not successful as the simulation did not stay numerically stable for even larger cohesion energy densities for which we also could not observe arching at this opening size. We note in passing that our material is behaving considerably more cohesive than that used by Carr et al. [8] (they experimentally observed a non-arching case in a similar draw down box already for an opening width of 200 [mm], and were able to reproduce this with spheres).

Result of Calibration and Validation with Tetrapods
We subsequently used tetrapods which are four rigidly connected primary spheres with a diameter $d_p = 8\,[mm]$ arranged on a tetraeder-shaped skeleton. This skeleton was chosen to have a center-to-center distance of $2.5 \cdot d_p$, resulting into strongly interlocking particles (the skeleton was not participating in the contact detection, and hence was "invisible" to the primary spheres). The choice of tetrapods is motivated by the fact that they are the simplest non-spherical isotropic

three-dimensional object we can form with multiple spheres. Again, the shape of the bottom pile was the target for calibration, and the experiment with an opening size of 250 mm has been used as the calibration setup. As can be seen, arching is correctly reproduced (see Figure 6b versus 6c). At the same time the relative mass loss difference m_{rel} between the simulation and the average of the experiments was extremely small ($m_{rel,calib} = 0.62\%$).
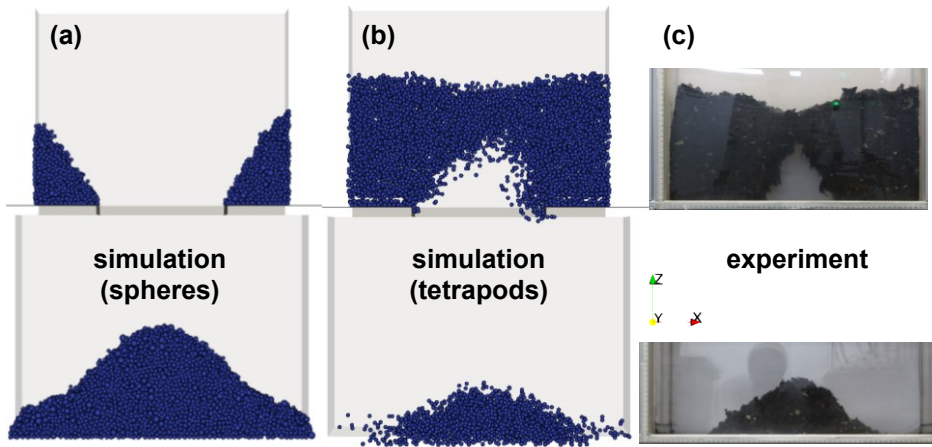

Figure 6. Illustration of the calibration procedure for an opening size of 250 mm using spheres (panel a; cohesion energy density $k_{sjkr} = 4 \cdot 10^5$ [J/m^3]) and tetrapods (panel b; cohesion energy density $k_{sjkr} = 3.1 \cdot 10^5$ [J/m³]), as well as a representative experimental result (panel c).

In order to validate the calibrated parameter set, we performed simulations with the tetrapods for two additional opening widths (see Figure 7), of course with identical DEM parameters as in the calibration case. Figures 7a1 and 7a2 show the results for a width of 320 [mm]. In 4 out of 6 experiments for this width arching occurred, i.e., this width represents a semi-stable case and is hence extremely difficult to reproduce. Indeed, our simulations predict a marginally stable arching situation (see Figure 7a1) with a reasonable (but certainly not excellent) match of the relative mass loss difference of $m_{rel} = 17.4\%$ (based on experimental data in which arching occurred). For the case of an extremely large opening width (i.e., 400 [mm], see Figures 7b1 and 7b2), we correctly predict the (almost completely) empty upper box that was observed in the experiment ($m_{rel} = 3.3\%$). Interestingly, also the shape of the pile is reasonably predicted (all 5 other realizations of the experiment yielded similar shapes of the pile).
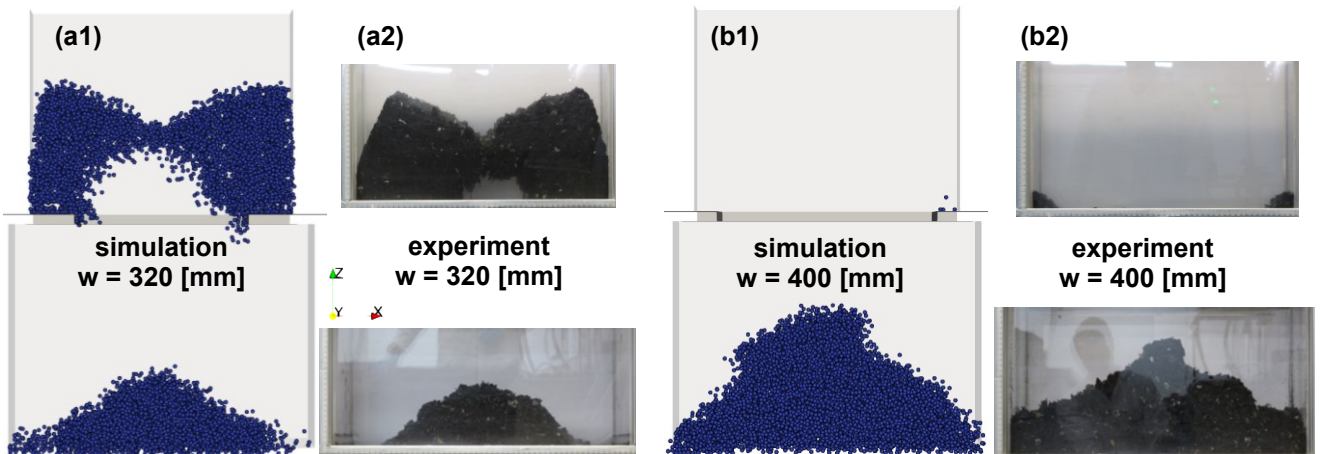

Figure 7. Validation of the calibrated tetrapod-based DEM model for different opening widths.

DEM parameters for NiMH Battery Recyclate Modeling - Heat Conduction
Unfortunately, it is extremely difficult to obtain measurements of the heat conductivity of the recyclate material. Also, such measurements are only meaningful if a controlled compaction state can be realized – this is because of the softness of the recyclate material. Due to these experimental difficulties, a direct calibration of the thermal properties of the recyclate was not possible. Furthermore, limitations in our

calibration software prohibited us from using the tetrapods - hence spherical particles were used only in what follows. Thus, we use this chapter to outline the difference of the bulk conductivity between the case with calibrated cohesion parameters (i.e., the already introduced SJKR model) and the case with no cohesion.

Setup and Postprocessing

The case setup used in the present chapter is a box with periodic boundaries in the lateral direction, and a stress-controlled wall at the top (see Figure 8, left panel). Particles are made of the same material (same density, same interaction parameters) as for our flow prediction in the previous chapter. We consider the calibrated value for the cohesion energy of $3.1 \cdot 10^5$ [J/m³]. We use the standard particle-particle and particle-wall heat conduction closure of Aspherix®, which assumes that heat conduction is proportional to the contact area between contacting particles.

Initially, the box is filled under gravity to a certain height. Particles are subsequently compressed with the desired normal stress σ_{zz}. During this compression step, and the subsequent heating of the box, gravity is disabled, since it would only induce an unwanted stress gradient in the system. When the desired stress is reached, the heating phase of the box starts. Note that the imposed normal stress is made dimensionless with the particle material's Young's modulus, i.e., $\sigma^* = \sigma_{zz}/Y$. Also, the cohesion parameter is made dimensionless in a similar way, i.e., $k_{sjkr}^* = \frac{k_{sjkr}}{Y}$.

At the top and at the bottom wall, two different temperatures are applied. For calculating the effective bed heat conductivity, the heat transfer through the walls is calculated from the simulation data. Furthermore, two boxes (a) and (b) (see the semi-transparent boxes in Figure 8, left panel) are initialized in which we track the average temperature of the particles that are located inside them.

Each simulation is run until the steady state is reached (see Figure 8, right panel; note that we defined a dimensionless time t^*, which is the ratio of the physical time and a thermal relaxation time scale of the bed given by $\tau_{relax,cond} = \frac{L_{Bed}^2}{a_{H,Bed}}$. In this relation L_{Bed} is the bed height, and $a_{H,Bed}$ is the heat diffusivity in the particle bed). As depicted in Figure 8 (the right panel), the steady state is reached after approximately 1.2 dimensionless time units. The effective bed conductivity changes by two orders of magnitude before this state is reached due to transient effects.
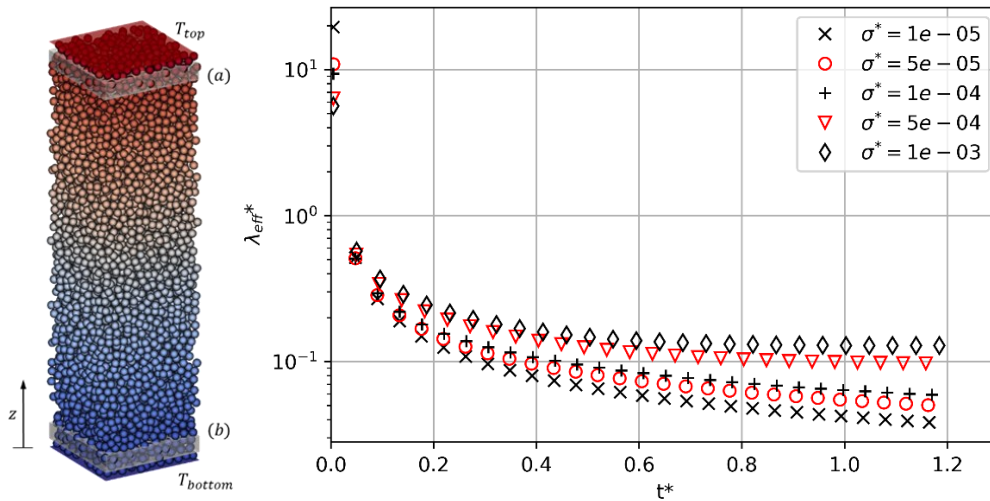

Figure 8. Snapshot of a heat conduction simulation (left panel), and typical transients of the measured effective heat conductivity for the case with cohesion with $k_{sjkr}^* = \mathbf{3.1 \cdot 10^{-3}}$.

Results

We report the main result as a dimensionless heat conductivity $\lambda_{eff}^* = \frac{\dot{Q}_{Sim}}{\dot{Q}_{ref}} = \frac{\lambda_{eff}}{\lambda_p}$ (λ_p is the particle material's heat conductivity) which is probed by dividing the measured the heat flux thru the walls (and hence thru the domain) with the negative temperature gradient. When calculating the latter, we found that it is important to use the average particle temperatures in the boxes (a) and (b), and not the wall temperatures (the latter would induce a considerable error, since the bed-wall heat transfer resistance is relatively large compared to the bed-internal heat conduction resistance).

Following Figure 9, we see that the effective heat conductivity varies considerably with the applied stresses onto the box. As expected, cohesion leads to a lower heat conductivity, since the particles form a structured network leading to a more porous bed at the same applied stress. We note in passing that also the particle volume fraction ϕ_p in the bed varies with the stress level (for the cohesionless system we observe small fluctuations around $\phi_p \approx 0.53$. In contrast, for the calibrated cohesive particles ϕ_p increases from 0.490 to 0.529 for a dimensionless stress change from $1\cdot10^{-5}$ to $5\cdot10^{-3}$). It is hence important to consider both (i) calibrated mechanical DEM model parameters and (ii) the applied stress level when learning thermal DEM parameters from experimental data.
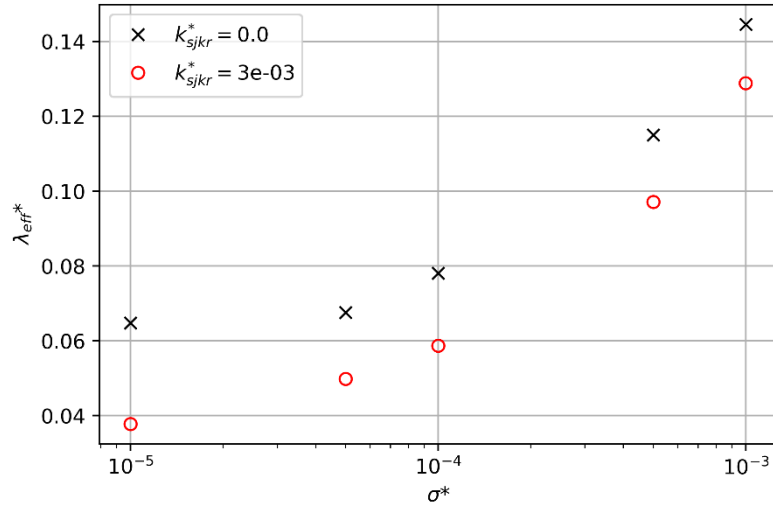

Figure 9. Influence of the normalized stress on the effective heat conductivity of the non-cohesive (black crosses) and cohesive calibrated material (red circles).

Summary

Various machine learning strategies have been practiced in the field of CFD-DEM simulations relevant for combustion processes. Learning hereby typically means that closure parameters (e.g., view factors in radiation modeling, a correction to the drag force, or DEM parameters) are iteratively determined via a computer algorithm based on experimental data, or simulated reference data. The subsequent validation of the trained model is essential – otherwise machine learning might be seen as a "parameter tuning" exercise with limited generality.

Which strategy for learning is most promising dependents on the application area, the complexity of the learning exercise (i.e., the number of markers that need to be used) and the amount of data to be handled. We have adopted a grey-box approach for view factor and drag modeling with good success: the trained models are robust enough against abuse and allow extrapolation.

When moving into the field of DEM parameter learning or calibration, we found that tetrapods are a potentially good choice for strongly cohesive systems. Our tetrapods do not add significant computational overhead, as their primary spheres do not overlap (and hence there is no "volume loss" when applying the multi-sphere approach). From our study it is also clear that any calibration of thermal DEM parameters needs to (i) rely on a prior calibration of mechanical parameters (e.g., for cohesion) and (ii) must consider a whole range of particle stress levels. Which stress levels are relevant needs to be known prior to such calibration tasks – predicting the stress level might be another interesting machine learning exercise.

As an outlook, we would like to mention that there is still a considerable amount of work going into the handling of data (for experimental, simulation, and calibration tasks). As a potential relief, we have recently invested in the development of a novel open-source workflow environment that will reduce this work at least for the calibration step (https://github.com/n-ghods/DEMvironment). Finally, the topic of heat conduction (and radiative transport) in cohesive granular materials - modelled with a coarse-grained multi-sphere approach - needs more attention in the future.

References

[1]   J. Tausendschön, G. Stöckl, S. Radl, Machine Learning for heat radiation modeling of bi- and polydisperse particle systems including walls, Particuology. 74 (2023) 119–140. https://doi.org/10.1016/j.partic.2022.05.011.

[2]   J. Tausendschön, S. Sundaresan, M. Salehi, S. Radl, Machine Learning-Based Filtered Drag Model for Cohesive Gas-Particle Flows, Chem Eng Technol. 46 (2023) 1373–1386. https://doi.org/10.1002/ceat.202300040.

[3]   E.I. Mahiques, M. Brömmer, S. Wirtz, B. van Wachem, V. Scherer, Simulation of Reacting, Moving Granular Assemblies of Thermally Thick Particles by Discrete Element Method/Computational Fluid Dynamics, Chem Eng Technol. 46 (2023) 1317–1332. https://doi.org/10.1002/ceat.202200520.

[4]   S. Radl, C. Radeke, J.G. Khinast, S. Sundaresan, Parcel-Based Approach for the Simulation of Gas-Particle Flows, in: 8th International Conference on CFD in Oil & Gas, Metallurgical and Process Industries, SINTEF/NTNU Trondheim, Norway, Trondheim, Norway, 2011: pp. 124 (1–10).

[5]   J.C. Wurzenberger, S. Wallner, H. Raupenstrauch, J.G. Khinast, Thermal Conversion of Biomass: Comprehensive Reactor and Particle Modeling, AIChE Journal. 48 (2002) 2398–2411.

[6]   W. Ketterhagen, C. Wassgren, A perspective on calibration and application of DEM models for simulation of industrial bulk powder processes, Powder Technol. 402 (2022). https://doi.org/10.1016/j.powtec.2022.117301.

[7]   C.J. Coetzee, O.C. Scheffler, Review: The Calibration of DEM Parameters for the Bulk Modelling of Cohesive Materials, Processes. 11 (2023). https://doi.org/10.3390/pr11010005.

[8]   M.J. Carr, T. Roessler, P.W. Robinson, H. Otto, C. Richter, A. Katterfeld, C.A. Wheeler, Calibration procedure of Discrete Element Method (DEM) parameters for wet and sticky bulk materials, Powder Technol. 429 (2023). https://doi.org/10.1016/j.powtec.2023.118919.

[9]   M. Ajmal, T. Roessler, C. Richter, A. Katterfeld, Calibration of cohesive DEM parameters under rapid flow conditions and low consolidation stresses, Powder Technol. 374 (2020) 22–32. https://doi.org/10.1016/j.powtec.2020.07.017.

[10]   W. Chen, T. Donohue, K. Williams, A. Katterfeld, T. Roessler, Iron Ore 2015 Conference Paper Number: 105 Modelling cohesion and adhesion of wet sticky iron ores in discrete element modelling for material handling processes, n.d.

[11]   K. Agrawal, P.N. Loezos, M. Syamlal, S. Sundaresan, The role of meso-scale structures in rapid gas–solid flows, J Fluid Mech. 445 (2001) 151–185. https://doi.org/10.1017/S0022112001005663.

[12]   S. Radl, S. Sundaresan, A drag model for filtered Euler-Lagrange simulations of clustered gas-particle suspensions, Chem Eng Sci. 117 (2014) 416–425. https://doi.org/10.1016/j.ces.2014.07.011.

[13]   Y. Jiang, J. Kolehmainen, Y. Gu, Y.G. Kevrekidis, A. Ozel, S. Sundaresan, Neural-network-based filtered drag model for gas-particle flows, Powder Technol. 346 (2019) 403–413. https://doi.org/10.1016/j.powtec.2018.11.092.

[14]   L.T. Zhu, X.Z. Chen, B. Ouyang, W.C. Yan, H. Lei, Z. Chen, Z.H. Luo, Review of Machine Learning for Hydrodynamics, Transport, and Reactions in Multiphase Flows and Reactors, Ind Eng Chem Res. 61 (2022) 9901–9949. https://doi.org/10.1021/acs.iecr.2c01036.

[15]   J. Tausendschön, Physics-based deep learning for advanced multiphase flow prediction, Graz University of Technology, 2023. https://repository.tugraz.at/marc21/y7xnf-5mz21 (accessed November 23, 2023).

[16]   L. Roeder, Netron, (2023). https://github.com/lutzroeder/netron (accessed November 23, 2023).

[17]   J. Tausendschön, S. Radl, Deep neural network-based heat radiation modelling between particles and between walls and particles, Int J Heat Mass Transf. 177 (2021). https://doi.org/10.1016/j.ijheatmasstransfer.2021.121557.

[18]   C.J. Coetzee, O.C. Scheffler, Review: The Calibration of DEM Parameters for the Bulk Modelling of Cohesive Materials, Processes. 11 (2023). https://doi.org/10.3390/pr11010005.

[19]   J. Schindelin, I. Arganda-Carreras, E. Frise, V. Kaynig, M. Longair, T. Pietzsch, S. Preibisch, C. Rueden, S. Saalfeld, B. Schmid, J.Y. Tinevez, D.J. White, V. Hartenstein, K. Eliceiri, P. Tomancak, A. Cardona, Fiji: An open-source platform for biological-image analysis, Nat Methods. 9 (2012) 676–682. https://doi.org/10.1038/nmeth.2019.

[20]   S. Amberger, S. Pirker, Models , algorithms and validation for opensource DEM and CFD-DEM Christoph Kloss *, Christoph Goniva , Alice Hager , 12 (2012) 140–152.

[21]   C. Kloss, LIGGGHTS(R)-Public Documentation , Version 3.X, (2015).

[22] T. Roessler, C. Richter, A. Katterfeld, F. Will, Development of a standard calibration procedure for the DEM parameters of cohesionless bulk materials – part I: Solving the problem of ambiguous parameter combinations, Powder Technol. 343 (2019) 803–812. https://doi.org/10.1016/j.powtec.2018.11.034.